

Removing the effects of task-related motion using independent-component analysis

Takanori Kochiyama,^a Tomoyo Morita,^a Tomohisa Okada,^b Yoshiharu Yonekura,^c Michikazu Matsumura,^a and Norihiro Sadato^{b,d,*}

^aGraduate School of Human and Environmental Studies, Kyoto University, Kyoto, Japan

^bNational Institute for Physiological Sciences, Okazaki, Japan

^cBiomedical Imaging Research Center, Fukui Medical University, Fukui, Japan

^dJST (Japan Science and Technology Corporation) / RISTEX (Research Institute of Science and Technology for Society), Kawaguchi, Japan

Received 18 May 2004; revised 4 December 2004; accepted 10 December 2004

Available online 12 February 2005

Task-related motion is a major source of noise in functional magnetic-resonance imaging (fMRI) time series. The motion effect usually persists even after perfect spatial realignment is achieved. Here, we propose a new method to remove a certain type of task-related motion effect that persists after realignment. The procedure consists of the following: the decomposition of the realigned time-series data into spatially-independent components using independent-component analysis (ICA); the automatic classification and rejection of the ICs of the task-related residual motion effects; and finally, a reconstruction without them. To classify the ICs, we utilized the associated task-related changes in signal intensity and variance. The effectiveness of the method was verified using an fMRI experiment that explicitly included head motion as a main effect. The results indicate that our ICA-based method removed the task-related motion effects more effectively than the conventional voxel-wise regression-based method. © 2004 Elsevier Inc. All rights reserved.

Keywords: Voxel; Motion; Regression; Functional MRI; Independent-component analysis (ICA)

Introduction

This paper describes a new method of adjusting functional magnetic-resonance imaging (fMRI) time-series data to remove the confounding effects of task-related subject movement (task-related motion effect).

In fMRI, it is common to collect a sequence of multi-slice images of the brain every few seconds. Changes in signal intensity that are related to task changes are used to infer functional

anatomy, usually on a voxel-by-voxel basis. The largest source of variance in fMRI time-series data is movement during the scanning session (Friston et al., 1995a). Over 30–90% of the variance in the MR signal can be attributed to movement (Friston et al., 1996). If untreated, the movement-related variance decreases the sensitivity of detecting the task-related changes. The first approach to solving this problem was to simply move the images back into register (rigid-body realignment) (Friston et al., 1995a). Even after perfect realignment, however, the residual effects of subject motion (residual motion effects) might still be present in the time series data. There are several sources of these motion-related artifacts (Ashburner and Friston, 1999), including spin-history effects (Friston et al., 1996), through-plane head motion (Lee et al., 1998), the interaction effect between magnetic-field inhomogeneities and the movements of subjects (Andersson et al., 2001), and the interaction effects among them. Interpolation errors are an additional source of residual motion effects (Grootoonek et al., 2000). In this paper, we use the term ‘motion effect’ to refer to the residual motion effect after correction for misalignment using a rigid-body transformation.

One possible solution to correct these motion effects in time-series data has been proposed in the framework of the univariate general linear model (GLM): the motion effects in each voxel were modeled by a nonlinear function of position in the current and previous scans, and these were covaried out of the time-series data as nuisance effects (Friston et al., 1996). However, this approach has a serious limitation: if task-related signal changes (true activations) are correlated with head movements, this component will be removed (Friston et al., 1996). This situation is likely to occur in experiments in which some conditions might cause slight head movements (such as motor tasks or speech) because these movements are often highly correlated with the experimental design (Ashburner and Friston, 1999). Hence, corrections for task-related motion effects are particularly difficult; without correction, there is a risk of an increase in pseudo-activations or false-positive (FP) errors, and with correction there is a risk of an increase in

* Corresponding author. Section of Cerebral Integration, Department of Cerebral Research, National Institute for Physiological Sciences, Myodaiji, Okazaki, Aichi, 444-8585 Japan. Fax: +81 564 55 7786.

E-mail address: sadato@nips.ac.jp (N. Sadato).

Available online on ScienceDirect (www.sciencedirect.com).

false-negative (FN) errors. This can be seen as a case of ‘throwing the baby out with the bathwater’ (Friston et al., 1996).

The difficulty stems partly from the temporal constraints of univariate time-series analysis with GLM; that is, orthogonality between the signals of interest and those that are not of interest. To be free from this constraint, the use of independent-component analysis (ICA) has been proposed. ICA is a multivariate statistical technique that can decompose fMRI data into spatially-independent components with associated time courses that are blind to temporal information (McKeown et al., 1998a,b). ICA can separate spatially the processes related to neuronal activity and the motion-artifact processes into different ICs if they have mutually different spatial distributions, regardless of the temporal orthogonality among them. Previous reports have suggested that neuronal responses, and various other physiological and physical processes, are not likely to overlap spatially and are expected to be regionally specific because there are different regional origins for each of the processes (McKeown et al., 1998a,b). A drawback of this approach was the absence of explicit criteria for characterizing each IC.

Here, we propose a new procedure to remove the effects of task-related motion from realigned fMRI time-series data, based on ICA. We made two explicit criteria for characterizing task-related motion effects, including the task-related changes in the signal intensity and its variance. We begin by presenting the theory and procedure, followed by an example of how it can be applied to real data that include a motion component as part of the task. We then evaluate the effectiveness of the proposed procedure.

Methods

Theory and procedures

The algorithm consisted of three steps: first, ICA decomposition of the realigned time-series data of the brain images; second, characterization of the ICs; and third, reconstruction of the imaging data, in which only the ICs that satisfied the criteria were re-projected onto the original image space. Schematic representations of our correction procedures are presented in Fig. 1. As Steps 1 and 3 are well-documented procedures (see Appendix A), we focus mainly on Step 2. Although these should be performed as preprocessing steps before statistical analysis, knowledge of the experimental design is necessary to select the ICs of interest.

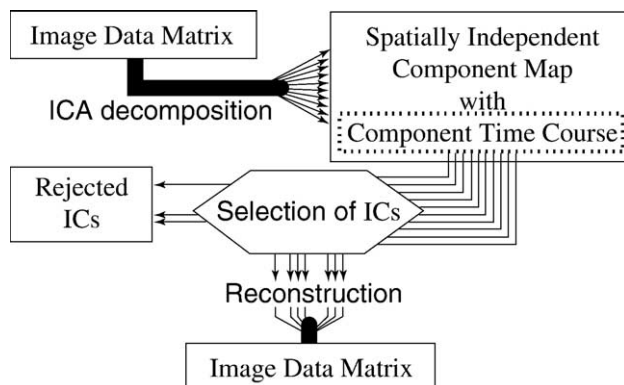


Fig. 1. Schematic representation of our correction procedure: Step 1, ICA decomposition; Step 2, selection of ICs; and Step 3, data reconstruction.

Step 1: ICA decomposition

The procedure of ICA decomposition is predominantly based on the work of McKeown et al. (1998a,b). The algorithm was based on the fast ICA (Hyvarinen, 1999; Hyvarinen and Oja, 2000).

Preprocessing

In each single session, the time-series data of all intracranial voxels were included in a data matrix, \mathbf{X} ; this was an n by m rectangular matrix, with n being the number of time points in a session and m being the total number of voxels sampled. To decrease the computational complexity of the ICA algorithm, data were centered (mean of zero) and whitened (sphering) to make each uncorrelated (orthogonalization) before running the ICA algorithm.

Decomposition

ICA assumes that spatially-independent components, \mathbf{C} , are derived from the data matrix, \mathbf{X} , by linear decomposition with an unmixing matrix, \mathbf{W} :

$$\mathbf{C} = \mathbf{W}\mathbf{X} \quad (1)$$

Here, \mathbf{C} is an n by m rectangular matrix, with n being the number of ICs and m being the total number of voxels, and \mathbf{W} is an n by n square matrix of full rank. Once the ICA algorithm was converged, we obtained n spatially-independent component maps as each row of $\mathbf{C} = \mathbf{W}\mathbf{X}$ and also calculated the mixing matrix $\mathbf{M} = \mathbf{W}^{-1}$, which represents the associated time course of each spatially-independent component map.

Step 2: Characterization of ICs

To classify the components containing task-related motion effects, we performed an F test based on a GLM and a Breusch–Pagan (BP) test (Breusch and Pagan, 1979). The former was employed to evaluate the task-related change in the signal intensity (as used in SPM99; see Appendix B for details). The latter was used to evaluate the task-related change in the variance of the time course of each component (see Appendix C for details).

Tasks are often accompanied through movement in response to the task demands; hence, repetitive task-related movements might result in head movement during the task-on phases. As a brief head movement causes a spike-like signal-intensity change with a short duration and large amplitude (Birn et al., 1999), we expected that motion effects during the task-on phases would be characterized by an increase in signal intensity and its variance compared with the task-off phases: the former can be evaluated by an F test and the latter by a BP test. Both tests can easily be applied to neuroimaging data in the framework of the GLM with least-square estimation.

We now briefly describe how the newly introduced BP test works in our methods (see Appendix C for general and mathematical explanations). The hierarchical regressions are sequentially performed both on the time course of an IC and on the residual time course of the first regression.

The first regression,

$$\bar{\mathbf{Y}} = \mathbf{G}\bar{\boldsymbol{\beta}} + \bar{\boldsymbol{\tau}} \quad (2)$$

is used to estimate the error of the time course, $\bar{\boldsymbol{\tau}}$, where \mathbf{G} is the design matrix of this regression, and $\bar{\mathbf{Y}}$ is a vector of the time series of an IC. The design matrix of the first regression usually

contains a set of regressors that model the task-related hemodynamics and monotonous low-frequency trends (for example, Fig. 2a). Note that in the first regression, we only take into account an increase in amplitude; hence, \vec{u} contains task-related inhomogeneity of variance or heteroscedastic forms of variance. This non-constant variance can be examined by the second regression as follows:

$$\vec{p} = \hat{\vec{u}}^2 / \hat{\sigma}^2 \quad (3)$$

$$\vec{p} = \mathbf{Z}\vec{\alpha} + \hat{v} \quad (4)$$

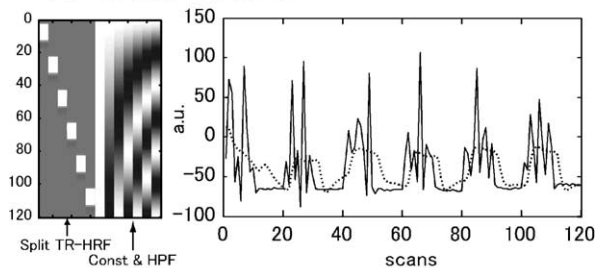
Here, $\hat{\sigma}^2$ is the variance estimated from the residual time series as follows:

$$\hat{\sigma}^2 = \hat{\vec{u}}^T \hat{\vec{u}} / n. \quad (5)$$

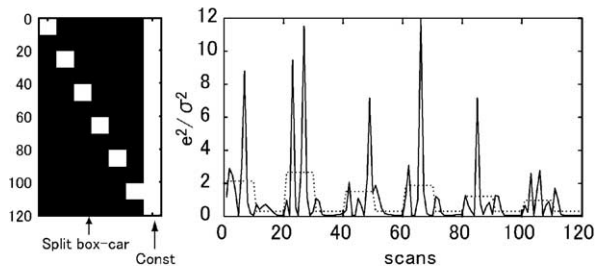
The second regression is conducted on the residual time series of the first regression (more correctly, the squared residual time series divided by its estimated variance). Here, design matrix \mathbf{Z} directly models the non-constant variance of the time series based

a) Breusch and Pagan test

(1) 1st step regression



(2) 2nd step regression



b) GLM F-test

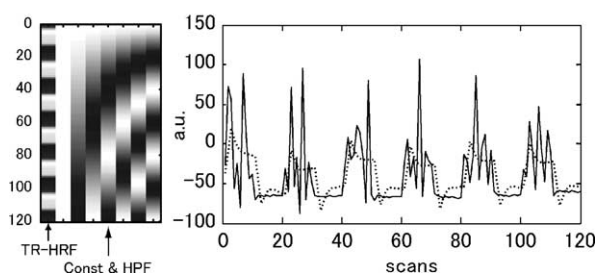


Fig. 2. Design matrix for the BP test (a) and the GLM F test (b), used when applying the procedure to real data. In the BP test, the first regression is performed only to estimate the residual time series for the second regression, and then the test statistics are calculated by the second regression. A sample component time course (solid line) and a fitted time course (dotted line) for each regression are also shown.

on our knowledge of the experimental design and the estimated realignment parameters. Generally, in an ordinary-blocked paradigm with several task-on and-off phases, \mathbf{Z} might consist of some separate rectangular functions (single box-car regressors) representing the duration of each task-on phase (for example, Fig. 2b).

Finally, test statistics that express how well the model \mathbf{Z} can explain the variance of the observations in the second regression—that is, the heteroscedasticity in the time course of an IC—are calculated. Based on χ^2 statistics, we can specify the appropriate threshold to evaluate the degrees of heteroscedasticity.

Step 3: Rejection of ICs and data reconstruction

In the final step, we reject the ICs caused by the task-related motion effects and reconstruct the data from the remaining ICs. The ICs, which are characterized by their correlation with the experimental design and the task-related heteroscedasticity in Step 2, are classified using the threshold of F and χ^2 statistics, respectively. Then, ICs showing both significant task-related signal change and task-related heteroscedasticity at the significance level of $P < 0.001$ are rejected. ICs passing these selection criteria are reconstructed to the corrected image matrix, which is derived as:

$$X' = MC' \quad (6)$$

Here, C' is the matrix of the corrected IC maps with the appropriate rows set to zero. A perfect image matrix is reconstructed by adding the row means.

Application to real data

Subjects and tasks

To evaluate the efficiency of our proposed method, finger-tapping tasks were performed with and without the presence of passive head movements synchronized with the task period.

Four right-handed normal male volunteers participated in our study. The protocol was approved by the Institutional Review Board of Fukui Medical University, Japan. All subjects gave their written informed consent.

The task consisted of two sessions: finger tapping without head motion (T+M−) and finger tapping accompanied by head motion (T+M+). The order of the sessions was pseudo-randomized among subjects. During the T+M− session, subjects were asked to perform a visually paced finger-opposition task for 30 s, alternating with 30 s of rest as a control condition. This was repeated six times. In the finger-opposition task, subjects performed a brisk and precise touch to the tip of the right thumb with the right index finger at a frequency of 1 Hz. The task and control epochs were cued by green- or red-colored stimuli, respectively, which blinked at a frequency of 1 Hz. Each of the task and control phases consisted of 10 images; hence, one session consisted of 120 images in total. The T+M+ session was the same as the T+M− session, except that the head motion was administered externally during the task phase via the pneumatic system described below. The generated head motion consisted of a nod-like movement, mimicking those that often appear during motor or speech tasks. This passive head movement was applied six or seven times during the task phase. The pneumatic system generated controlled movements of the head of the subject within the MRI scanner, in the manner of Field et al. (2000). An air cushion made of vinyl chloride (~26 cm long and ~12 cm wide) was spread under the head of the subject. The air cushion was connected to a foot-

operated air pump through a plastic tube, with a three-way stopcock inserted between the two. The head movement could be started and stopped promptly by operating the stopcock. The foot-operated air pump was controlled by one of the experimenters. The volume of air in the cushion was adjusted so that the head of the subject would move ~3–4 mm. Elastic padding was placed on both sides of the head of the subject and headbands were also used to stabilize the head. Using this system, combined with the biomechanical properties of the head, the inflation and deflation of the air cushion successfully allowed nodding movements. The frequency of movements was adjusted to 0.3–0.4 Hz. The actual movements applied to the subject during the task phase in the T+M+ session were checked retrospectively using realignment parameters estimated during the realignment process.

The subjects were instructed not to allow their attention to stray from the task, even if their head was moved. An experimenter confirmed the task performance of each subject.

MRI acquisition

Data were obtained with a 3-T MRI system (SIGNA Horizon, GE, Milwaukee, WI, USA) using a standard birdcage coil. A time-course series of 126 functional images for each session were acquired using a T2*-weighted gradient echo-planar sequence with a TR of 3000 ms, a TE of 30 ms and a flip angle of 90°. The first six volumes were discarded because of non-steady conditions of magnetization and the remaining 120 volumes were used in the following analysis. Each volume consisted of 24 slices with a slice thickness of 3.5 mm and a 0.5-mm gap to cover the entire brain. The field of view was 22 × 22 cm, and the matrix size was 64 × 64, giving voxel dimensions of 3.44 × 3.44 × 4.00 mm. Soon after the completion of the acquisition of all functional images, a T2-weighted high-resolution anatomical image was obtained using a fast-spin echo sequence with a TR of 6000 ms, a TE of 67 ms, a flip angle of 90°, a matrix size of 256 × 256, voxel dimensions of 0.859 × 0.859 mm and a total of 112 transaxial slices.

Data analysis

Image preprocessing

Image preprocessing was carried out with SPM99 software from the Wellcome Department of Cognitive Neurology (London, UK; <http://www.fil.ion.ucl.ac.uk/spm>). The functional images from each subject were realigned using the last image as a reference. For this registration, six parameters (three translations and three rotations) were extracted from the rigid-body transformation that minimized the difference between each image and the reference (Friston et al., 1995a). After registration, all images were resliced using a sinc interpolation. Motion effects were corrected firstly by our proposed ICA procedures, and secondly by covarying out the effects using a multiple-regression analysis based on Friston et al. (1996). This was done only for the images acquired during the T+M+ session. Finally, all functional images were smoothed spatially with an isotropic Gaussian kernel of 6 mm. A T2-weighted high-resolution MRI was co-registered with the last functional image. These procedures were similar to those commonly used in fMRI experiments.

ICA correction of motion effects

The application of the ICA correction was performed as explained above. First, we specified three design matrices: one

for the GLM F test to evaluate the relationship between the IC waveform and the experimental design, and two for the BP-test to check the heteroscedasticity of the IC waveform. For the GLM F test, we adopted the same design matrix, which was used in the subsequent statistical analysis for the construction of the SPM{T}: the task-related signal-intensity change was modeled with a box-car function convolved with a canonical hemodynamic-response function. We used the discrete cosine basis function with a cut-off period of 120 s as a high-pass filter (Fig. 2b). The threshold for rejection on the GLM F test was set to $P < 0.001$. The BP test involves two steps of multiple regression: one performed on the time-series data of each IC, and one performed on the residual time series estimated in the first regression. For the first regression, we adopted the design matrix that contained six task-related box-car functions convolved with a canonical hemodynamic-response function and a discrete cosine basis function with a cut-off period of 120 s as a high-pass filter (Fig. 2a(1)). In this regression, we split the single task-related box-car function into six task period-related ones, which prevented the signal-intensity change between repetitions of the task from contaminating the residual time series and causing task-related systematic changes. For the second regression, the design matrix contained six task-related box-car functions and a constant. The threshold for rejection for the BP test was $P < 0.001$.

Statistical analysis

The task-related blood-flow change represented by the blood oxygen level-dependent (BOLD) signal was modeled with a box-car function convolved with a canonical hemodynamic-response function. We applied the discrete cosine basis function with a cut-off period of 120 s for the high-pass filter and the Gaussian kernel of 4 s for the low-pass filter (Friston et al., 1994, 1995b, 2000; Worsley and Friston, 1995). A pre-planned comparison was performed to test the significance of the increased activation related to the finger-opposition effects and the head movements using the appropriate linear contrast. We then constituted the statistical parametric map of the T-statistic SPM{T}.

Comparison with the conventional analysis method and evaluation of the new procedure

To evaluate the efficiency of our procedure, an identical data set was treated with the conventional voxel-by-voxel multiple-regression approach (Bullmore et al., 1999; Friston et al., 1996), in which the motion effects were modeled and covaried out using a first-order auto-regressive model of the realignment parameters and their squares (a total of 24 regressors: six realignment parameters, six of their squared time courses, and each of six derivatives of the realignment parameters or their squares).

We then performed modified receiver-operating characteristic (ROC)-based analysis (Lee et al., 1998) to examine the efficiency of our procedure and to compare it with the conventional approach. A ROC graph has a two-dimensional axis that describes the true-positive fraction (TPF) and the false-positive fraction (FPF). In our experiment, the TPF was the ratio of the activated areas during the T+M+ session within the ‘true’-activation areas found during the T+M– session.

In all four subjects, the true-activation areas were located in the left-hemisphere digit areas of the primary sensorimotor cortex, SMA (supplementary motor area) and right cerebellum (Fig. 6).

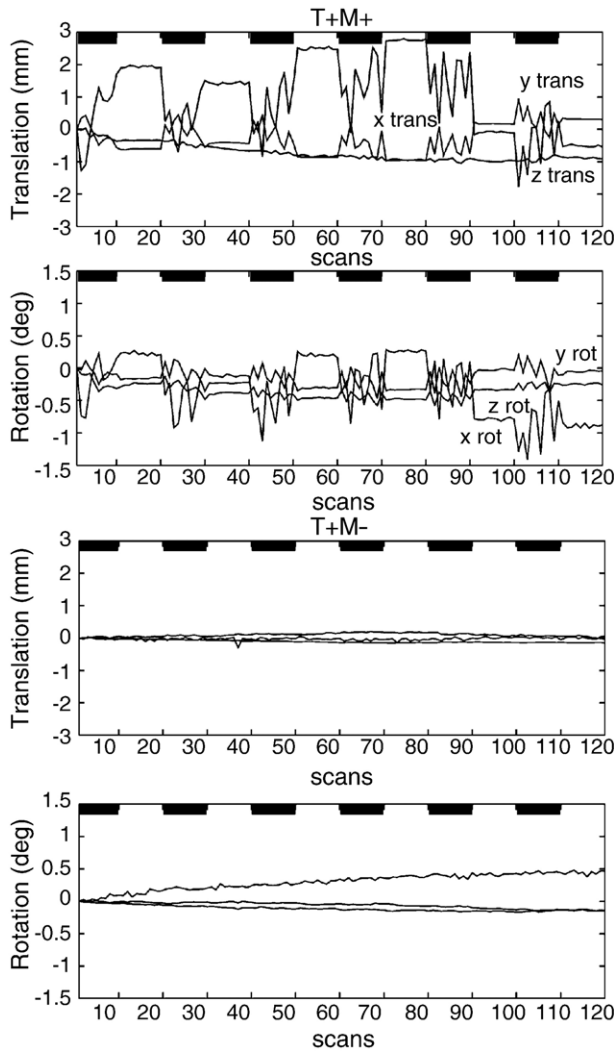


Fig. 3. The estimated realignment parameters of a representative subject are shown. In the T+M+ session, the time course of the realignment parameters was synchronized with the task cycle: $r = 0.41 \pm 0.14$ (mean correlation coefficient (\pm SEM) for X translation; $r = -0.42 \pm 0.15$ for Y translation; $r = -0.38 \pm 0.13$ for X rotation; and $r = -0.34 \pm 0.11$ for Y rotation.

The FP activity was defined as activation that was seen outside the true-activation areas (pseudo-activation).

As the extent of the TP areas depended on the statistical threshold of the $SPM\{T\}$, we varied the $SPM\{T\}$ threshold from $P < 0.0001$ to <0.05 , and then calculated the TPF and FPF to create the ROC graph. First, we defined the true-positive volume of interest (TP-VOI) of the T+M- session with the $SPM\{T\}$ threshold set at $P < 0.001$. Next, the TPF was defined as the ratio of the number of voxels above the threshold and inside the TP-VOI, compared to the total number of voxels in the TP-VOI. Here, the threshold was selected from one of the following values: $P < 0.0001$, <0.005 , <0.001 , <0.01 , or <0.05 . The FPF was defined as the ratio of the number of voxels exceeding the threshold inside the cranium but outside TP-VOI, compared to the total number of voxels in the whole brain minus those in TP-VOI (Lee et al., 1998).

A set of TPF and FPF values for the corrected data at the various thresholds was normalized using the initial values of TPF and FPF calculated from the non-corrected data. This process was

performed for every subject. Finally, the normalized TPF and FPF values were averaged over the four subjects, and plotted with the TPF on the X axis and the FPF on the Y axis to create the ROC graph. The more accurate the method is, the closer its ROC curve shifts towards the upper left corner of the graph.

Results

Characteristics of head motion

The head movements of each session for each subject were confirmed retrospectively using the estimated realignment parameters (Fig. 3). Head movements that were synchronized with the task cycle were seen principally in the realignment parameter of translation in the X (left–right) and Y (anterior–posterior) directions, and rotation around the X and Y axes during the T+M+ session. No such correlation was seen during the T+M- session. This tendency was observed in all subjects (Table 1). The amplitude of the Y-translation and X-rotation in the T+M+ session was, however, about twice as large as that of the X translation and Y rotation, respectively. Hence, the task-related nodding head movements were those that were artificially generated by the pneumatic system. The artificial head movement introduced obvious fluctuations of the realignment parameters during the task phase (Fig. 3), with an increase in the standard deviation (Table 1). This indicates that the head motion itself is heteroscedastic, which, in turn, introduced the task-related heteroscedasticity to the fMRI time series. This is useful when considering when our method should be applied.

Correcting the task-related motion effects

The following section is presented in two parts. The first verifies our criteria for the selection of the rejected ICs. We demonstrate that the ICs affected by the task-related motion effects

Table 1

The correlation between the estimated realignment parameters and the experimental design, and the standard deviations of task-on and task-off periods

	Correlation coefficient (\pm SEM)	Standard deviation (\pm SEM)	
		Task phase	Rest phase
<i>(a) M+T+</i>			
X translation	0.41 ± 0.14	0.32 ± 0.04	0.02 ± 0.00
Y	-0.42 ± 0.15	0.72 ± 0.12	0.04 ± 0.01
Z	0.14 ± 0.12	0.07 ± 0.02	0.04 ± 0.01
X rotation	-0.38 ± 0.13	0.31 ± 0.02	0.05 ± 0.01
Y	0.34 ± 0.11	0.13 ± 0.00	0.02 ± 0.00
Z	0.13 ± 0.10	0.08 ± 0.00	0.02 ± 0.00
<i>(b) M+T-</i>			
X translation	0.05 ± 0.07	0.01 ± 0.00	0.01 ± 0.00
Y	-0.06 ± 0.07	0.03 ± 0.01	0.03 ± 0.01
Z	-0.02 ± 0.09	0.03 ± 0.00	0.04 ± 0.01
X rotation	0.05 ± 0.05	0.03 ± 0.00	0.04 ± 0.00
Y	0.02 ± 0.06	0.01 ± 0.00	0.02 ± 0.00
Z	0.06 ± 0.07	0.01 ± 0.00	0.01 ± 0.00

Results were averaged over the four subjects. We confirmed that the movement applied by the pneumatic system correlated with the experimental design. Also shown is the variance inhomogeneity between the different task periods.

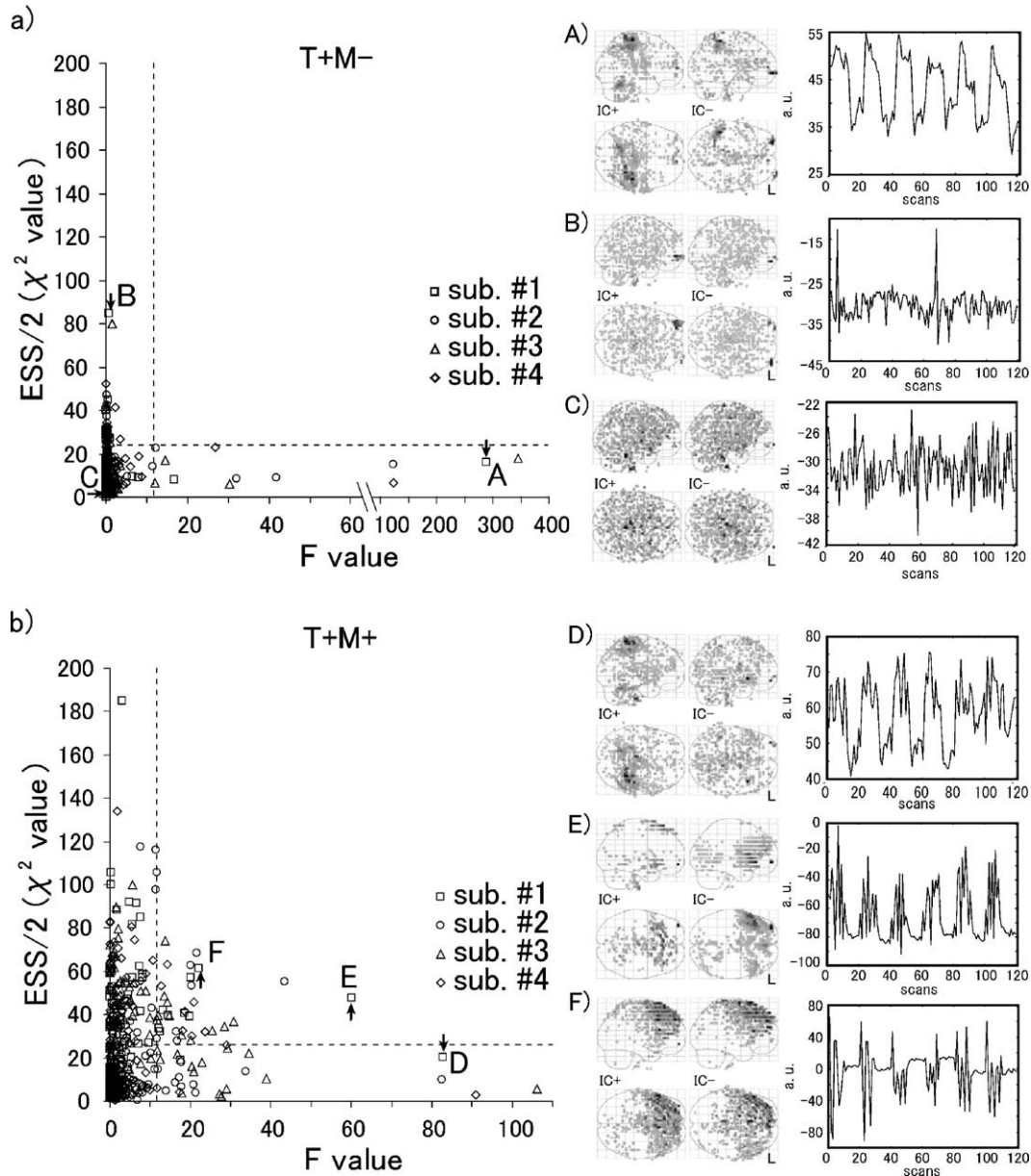


Fig. 4. (a) A scatter plot of ICs for T+M- sessions (without head motion), displaying their heteroscedasticity and task-correlation. The former was measured by ESS/2 of the BP test, and the latter by the F value of GLM for a task-related change. All of the ICs of all subjects, denoted by the different symbols, were plotted. The horizontal dashed line indicates the threshold of ESS/2 corresponding to $P = 0.001$, and the vertical dashed line indicates the threshold of F corresponding to $P = 0.001$. A (with vertical arrow) indicates an IC of subject 1 that shows high task-correlation and low heteroscedasticity, and hence was categorized as 'true' task-related activation. Its spatial distribution (Z-transformed IC map, top of the middle column) and time course (top of the right column) are depicted. The threshold of the Z-transformed IC maps was set to $|z| > 2$ for display purposes (McKeown et al., 1998a,b). IC+ and IC- denote the spatial distribution of positively or negatively 'active' voxels, respectively. Note that the sensory motor area was the active region for this component. B (with vertical arrow) is a heteroscedastic but not task-related IC. Its spatial distribution includes the eyes (second row of the middle column), probably reflecting rapid and abrupt eye movements (second row of the right column). C (with vertical arrow) is a homoscedastic non-task-related IC, showing diffuse spatial and temporal patterns (third row of the middle and right column), as seen in previous reports (McKeown et al., 1998a,b). (b) A scatter plot of ICs for T+M+ sessions (with head motion). D (with vertical arrow) is an IC with high task-correlation and low heteroscedasticity. Its spatial distribution (fourth row of the middle column) is similar to A, but the temporal patterns in the task phase were more sluggish than A. E and F (with vertical arrows) are task-related heteroscedastic and task-related ICs. This type of IC was the main interest of our correction procedure.

can be discriminated using two independent measures: the F value for correlation with the experimental design, and one half of the ESS value for the task-related heteroscedasticity. The second part demonstrates, using the ROC graph, the efficacy of our method compared with the conventional method, which employs the voxel-by-voxel GLM framework (Friston et al., 1996).

Characterization of each IC

Task-related signal changes and their heteroscedasticity

Fig. 4 shows a scatter plot displaying the relationship between the ESS/2 (χ^2 value) of the BP test and the F value of the task-related effect of all ICs for four subjects, both for the T+M- (Fig.

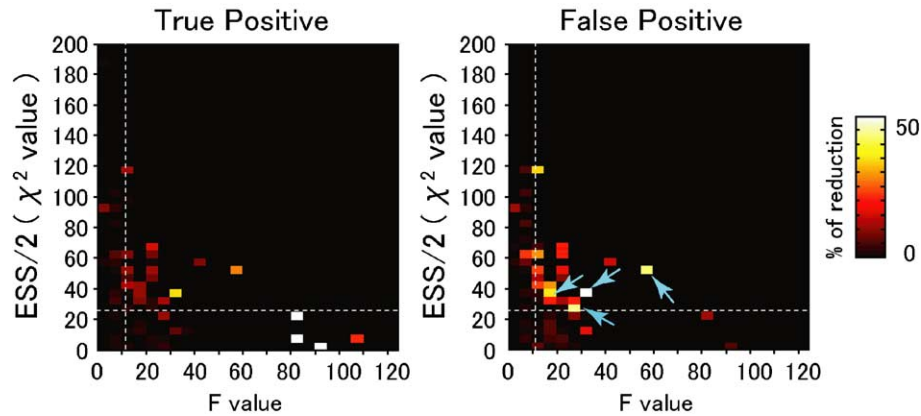


Fig. 5. (Left) The reduction in the sensory motor true-positive (TP) voxels by removing the IC. The percent reduction of TP voxels, indicated using a color scale, produced by removing an IC that was plotted against its heteroscedasticity (by means of EES/2) and task correlation (by means of F value). The horizontal dashed line indicates the threshold of EES/2 corresponding to $P = 0.001$, and the vertical dashed line indicates the threshold of F corresponding to $P = 0.001$. By removing the ICs with high task correlation and low heteroscedasticity, TP voxels were markedly reduced. (Right) The reduction in the false-positive (FP) voxels caused by the removal of the IC. Some ICs with high-task correlation and high heteroscedasticity (light-blue arrows) are responsible for up to 50% of the FP voxels.

4a) and the T+M+ (Fig. 4b) conditions. The distribution of the ICs for the head-motion session (T+M+) is more widespread than that of the session without head movements (T+M–). Note that the T+M+ session is characterized by ICs that have both task-related signal changes and task-related heteroscedasticity (the right and upper sides of the dotted line in Fig. 4b). This might be related to the pseudo-activation, as mentioned later. These problematic components had unique spatial distributions localized to CSF regions or at the edge of the brain. Furthermore, the time course of these components had task-related fluctuations and showed heteroscedasticity between the task and rest phases (for example, E and F in Fig. 4b). Their spatio-temporal patterns are different from the ICs that were highly correlated with the hemodynamic reference function with weak or no heteroscedasticity (for example, A in Fig. 4a), or those that were highly heteroscedastic without any correlation with the reference function (for example, B in Fig. 4a), both of which were observed in the sessions without head motion. Furthermore, the ICA succeeded in extracting the task-related ICs in the sessions with head motion (for example, D in Fig. 4b), the spatial distribution and temporal pattern of which were similar to the corresponding IC component during the T+M– session (for example, A in Fig. 4a). Only this component showed these characteristic features in all subjects.

Contribution of each IC to type-1 and -2 errors

We estimated the contribution of each IC to the artifactual pseudo-activations (type-1 errors) and to the reduction in the detection of true activations (type-2 errors). These were evaluated in terms of reducing the FP and TP voxels when removing an IC,

as follows: every time we removed a specific IC from the T+M+ session for each subject, we applied the same procedures as in the efficiency evaluation. The threshold of the SPM{T} was fixed to $P < 0.001$ (uncorrected). The resulting TPF and FPF values for the IC were compared with the TPF and FPF values of the non-removed cases. The percent reduction in TPF and FPF values was calculated and averaged within the cells defined by the rectangular lattice with class intervals of five for F values and five for ESS/2 values (χ^2 value). Fig. 5 shows the color chart of the averaged TPF or FPF reductions. The ICs contributing to TP activation showed high F values (>80 ; that is, high task synchronization) with lower ESS/2 values (<20 ; that is, lower task-related heteroscedasticity). According to Fig. 4b, these components represent the task-related brain activity, and hence should be preserved after component selection. However, the ICs contributing to FP activations showed both medium correlations (F value = 10–60) and marginally higher heteroscedasticity (ESS/2 = 20–70). Some ICs by themselves could reduce FP voxels by $>50\%$. Our established threshold for both tests can classify these ill-natured ICs (the vertical and horizontal dotted lines in Fig. 5). In this study, we successfully classified and preserved these components with the empirically defined threshold that we applied.

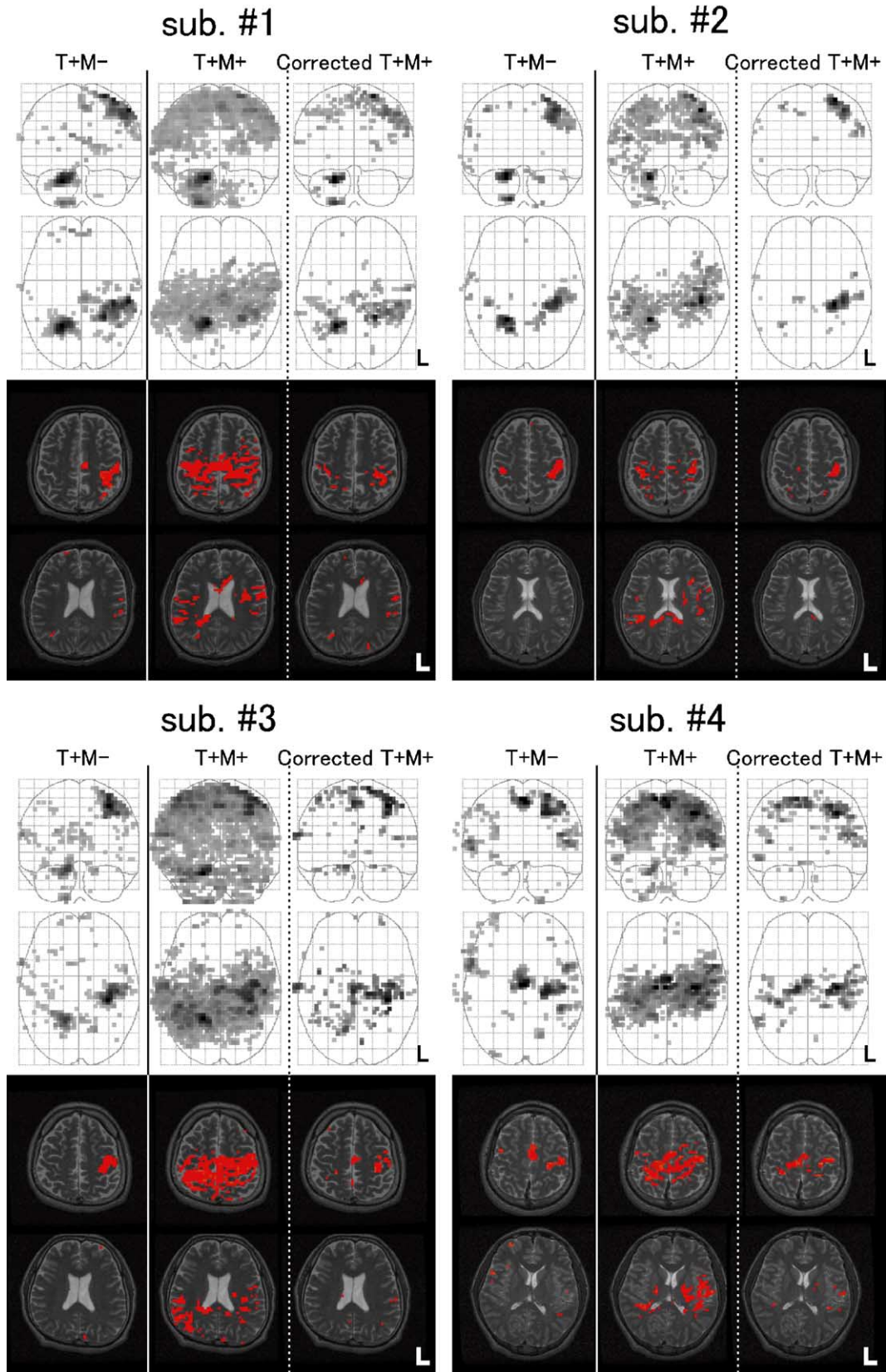
Reconstructed data

Fig. 6 illustrates the effect of the correction procedure on the empirically defined threshold of the GLM F test and BP test. For each subject, the maximum-intensity projection (MIP) images and the sectional images in the left column indicate the statistical results for the T+M– session (that is, the ideal goal of correction). The remaining columns indicate the statistical results of the non-

Fig. 6. Results of applying the method to real data. (Upper left) The statistical parametric maps SPM{T} of subject 1 for the T+M– session (left column), and the T+M+ sessions before (middle column) and after (right column) ICA corrections. The maximum-intensity projections (MIPs) viewed from the front (top row) and bottom (second row) are shown. Note that the MIP images are only for display purposes, as the images are not spatially normalized into Talairach space. The SPM{T} was superimposed on T2-weighted images of the subject (third and fourth rows). All SPM{T} thresholds were set to the significance level of $P < 0.001$. Subjects 2 (upper right), 3 (lower left) and 4 (lower right) are shown in the same format. Many pseudo-activated voxels in the T+M+ session disappeared after the ICA correction, while the active areas of corrected data were well preserved in the TP area.

corrected data (middle) and corrected data (right) for the T+M+ session. For the T+M- session, we found statistically significant activations in left SM1 and SMA, and right cerebellum (note that

the activation in SMA of subjects 2 and 3, and the cerebellum of subject 4 did not reach our threshold of $P < 0.001$) (Fig. 6, left column).



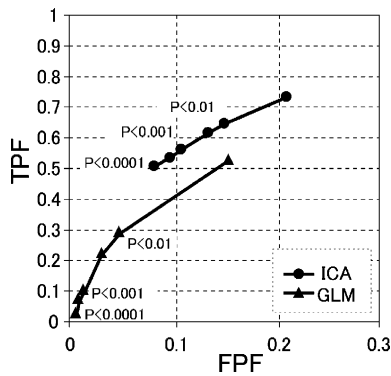


Fig. 7. The modified ROC curves of the correction for motion-related effects with ICA and GLM. The normalized false-positive fraction (FPF) and true-positive fraction (TPF) were plotted with different thresholds of $SPM\{T\}$ from $P < 0.0001$ (uncorrected) to < 0.05 (uncorrected). The curves were generated by averaging the results of the four subjects. The ROC curve of the ICA correction (closed circle) was located in the upper left portion of the graph, compared with the conventional method (GLM, closed triangle) (Friston et al., 1996), indicating a better performance.

For the non-corrected data from the T+M+ session, the distributed pseudo-activations severely obscured the TP activation (Fig. 6, middle column). After applying the ICA correction, almost all pseudo-activations disappeared, leaving the clusters of true activity only in the areas activated in the T+M– session (Fig. 6, right column). However, visible FNs (for example, losing some active clusters in the cerebellum for subject 2) were also observed at this threshold.

Efficiency evaluation

The performance efficiency of this method was evaluated in terms of the degree to which the FP (type-1) and FN (type-2) error rates changed when we successively moved the threshold of the $SPM\{T\}$ from $P < 0.0001$ (uncorrected) to < 0.05 (uncorrected). Fig. 7 summarizes the change in the FPF and TPF as a modified ROC graph, which displays the trade-off between the control of FP and the maintenance of TP. The goal of our correction was to reduce FP voxels while retaining as many TP voxels as possible. This was achieved if the points were located in the upper left portion of the ROC graph. Using the ROC graph, we also compared our procedure with a previous method employing a GLM framework (Friston et al., 1996).

The modified ROC graph shows that we could control the FPF at the 10% level while retaining ~55% of TP voxels when the statistical threshold of $SPM\{T\}$ was set to $P < 0.001$. At the same threshold, the regression-based method strongly

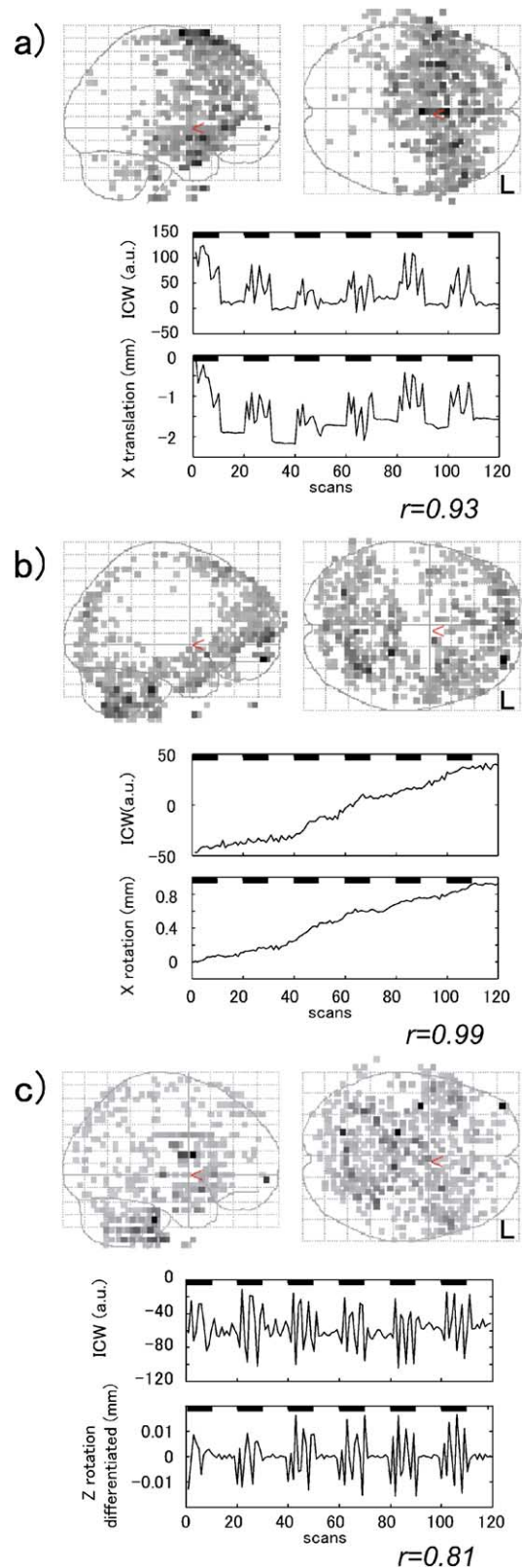


Fig. 8. (a) The spatial distribution (top row) and the waveform (second row) of the IC that correlated with the realignment parameter (x transition, third row). The maximum-intensity projections (MIP) viewed from right (top left) and from bottom (top right) are shown. Task-related changes and task-related heteroscedastic changes are evident (from subject 1 in the T+M+ session): a.u., arbitrary unit; ICW, independent component waveform; r , correlation coefficient. (b) ICW with low-frequency fluctuation correlated with the realignment parameter of the X rotation (from subject 2 in the T+M– session); and (c) with the temporal derivative of a realignment parameter (Z rotation differentiated) rather than itself (from subject 1 in the T+M+ session). These ICs have a peculiar spatial distribution with a ring-like configuration around the Y axis (a), or spreading widely over the edges of the brain (b) and CSF (cerebrospinal fluid) regions (c). From the correlation with realignment parameters in conjunction with the spatial distribution, we can infer that these ICs would be related to residual motion.

controlled FPF but lost almost all TP voxels, leading to FN errors. In Fig. 7, the ROC curve of our ICA procedure is always located in the upper left portion of the graph when compared with that of the approach used previously. This indicates that the ICA procedure maintains better control of both type-1 and-2 errors than the regression-based method (Friston et al., 1996).

Discussion

In this study, we presented a new approach to the removal of task-related motion effects from realigned fMRI time series. This novel method led to fewer FN errors compared with previous approaches. The crucial aspects of our procedure included the utilization of ICA to decompose the fMRI data using explicit criteria to characterize the ICs of the task-related motion, such as the task-related change in signal intensity and its variance (heteroscedasticity).

ICA is a well-established method that can be applied to various functional neuroimaging modalities, including fMRI (Arfanakis et al., 2000; Biswal and Ulmer, 1999; Calhoun et al., 2001, 2002; Duann et al., 2002; McKeown et al., 1998a,b; Moritz et al., 2000). It is assumed that the spatio-temporal fMRI dynamics consist of one or more spatially-independent processes, which originate in various physiological and physical mechanisms, such as hemodynamics, image artifacts, machine noise and head motion (McKeown et al., 1998a,b). With this assumption, the ICA algorithm can decompose these processes linearly into spatially-independent components, each associated with a single time course and component map. The spatial independence of the motion-related process is acceptable because the motion-related signal changes are caused by a different mechanism to the other processes. Some reports have demonstrated that ICA decomposes motion-suspicious ICs that map with spatially-inhomogeneous distributions; for example, if the focus preferentially lies on boundaries between different tissues or at the edge of a slice (McKeown et al., 1998a,b; Moritz et al., 2003), and the time course closely matches one of the estimated realignment parameters (for example, Fig. 8; also, see Bannister et al., 2001). This phenomenon was observed in both non-realigned fMRI data (McKeown et al., 1998a,b) and a realigned data set (Moritz et al., 2003). In the present study, we found several components that revealed typical artifact distribution around the edge of the brain and ventricles, which was more prominent in the T+M+ data than in the T+M– data, both of which were spatially realigned (Fig. 4). We confirmed that ICA is sensitive enough to detect motion-related processes, supporting the idea that ICA might be used as a correction tool for motion effects.

Although ICA is a data-driven analytical technique and does not rely on strong a priori assumptions regarding the time courses of the spatially-independent components, subsequent interpretation and classification of the separated components is required (McKeown, 2000). In this study, we introduced two measures for the automatic classification of the separated ICs: the task-related change in signal intensity and its variance. The latter was introduced on the basis of the observations of Birn et al. (1999). They demonstrated that the impulse response of a brief movement was characterized by a spike-like form with a short duration and large amplitude (rising at the same time as a movement and reaching its peak within a few seconds). These

could be temporally distinguished from prolonged hemodynamic responses (rising 1–2 s after a task and reaching a peak after 4–5 s) if an event-related paradigm was used (see Fig. 3 in Birn et al., 1999). This type of motion can be caused by, for example, jaw, tongue, facial muscle, or eye movements (Birn et al., 1998, 1999; Chen and Zhu, 1997; Yetkin et al., 1996) as well as global head motion during conditions when the head is restrained (see Seto et al., 2001). In a simple blocked paradigm contaminated by brief periods of motion, the characteristics of the motion-related signal changes reflect an increase in signal intensity and variance during the task-on phases compared with the task-off phases (see Figs. 2 and 4 in Birn et al., 1999). From this evidence, we expected that the time course of the motion-related IC would show the same characteristics. The results of the present study are consistent with this idea. We characterized all ICs using an F test to analyze the task-related increase in signal intensity and the BP test to assess the task-related serial inhomogeneity in variance (task-related heteroscedasticity). As a result, the number of ICs with task-related signal changes was larger in the session with head motion (T+M+) than without it (T+M–); the number of ICs with task-related heteroscedasticity showed a similar pattern (Fig. 4). Furthermore, according to Figs. 4 and 5, there were relatively few ICs with both of these characteristics, but they contributed greatly to the reduction in FP voxels. It is important that as few ICs as possible are removed in order to retain the degrees of freedom of the filtered data; therefore, the use of the BP test combined with the F test is appropriate, particularly with severely motion-contaminated data.

Fig. 7 shows the ROC analysis used to assess the efficiency of our procedure compared with a previous method. As previously mentioned, the method based on voxel-by-voxel linear-regression analysis caused a large decrease in specificity. We verified that our empirically specified threshold of $P < 0.001$ for both the BP test and the F test worked well in our simulation and when applied to data from other studies in our laboratory. In fact, the applied threshold ($P < 0.001$ for both the F test and BP test) was able to retain 55% of the TP voxels while suppressing FP errors to 10% in the T+M+ condition. Furthermore, in the T+M– condition, no IC component was falsely labeled as an ‘artifact’ at this threshold (Fig. 4). Considering that the task-related head movements simulated in this study were so extreme, a threshold of $P < 0.001$ for both the F test and BP test should work well in most situations. However, the confirmation of the optimal threshold requires further investigation, including a large number of simulations.

Caveats and limitations of the method

The proposed method necessitates knowledge of the movements of the subject, because the time windows when head movements preferentially occur are required by the second regression of the BP test. This can be achieved using the experimental design as well as the time course of the estimated motion parameters that are obtained through the realignment process. If the movement (by means of the estimated motion parameters) is not task-related, the conventional method of Friston et al. (1996) will work well. If the movement is task-related, our method can be applied.

Inspection of the estimated motion parameters is also important to the detection of motion effects that cannot be

estimated by the present method. For example, the subject might move at the start of a task-on phase, remain in the same position, and then return to the original position at the end of the task-on phase. In this case, the expected motion-related effects will consist of a box-car-like time series as previously simulated with a phantom model (Field et al., 2000). In this case, our method would fail to identify the motion-related ICs because of the lack of heteroscedasticity.

Theoretically, our method can process the motion effects in non-blocked paradigms if we can establish the design matrix of the second regression in the BP test. However, we need to further investigate how effectively our method, and particularly the BP test, can characterize motion-related ICs in non-blocked paradigms.

Acknowledgments

This study was supported by a Grant-in-Aid for Scientific Research B#14380380 (NS) from the Japan Society for the Promotion of Science, and Special Coordination Funds for Promoting Science and Technology from the Ministry of Education, Culture, Sports, Science and Technology, Japan. The authors would like to thank the subjects who participated in this study, and also the staff of the Biomedical Imaging Research Center and the Department of Radiology of Fukui Medical University, Japan, for their assistance with data collection.

Appendix A

ICA decomposition

The ICA decomposition procedure is based mainly on the work of McKeown et al. (1998a,b). Several methods for performing ICA decompositions have been proposed, which use different objective functions together with diverse criteria for the optimization of the objective functions. In this study, ICA decomposition was performed using two different algorithms: an information-maximization algorithm (Bell and Sejnowski, 1995) and a fixed-point algorithm known as a fast ICA (Hyvarinen, 1999), both of which were implemented in SPM99. These two algorithms are available on the Internet free of charge (<http://www.cnl.salk.edu> or <http://www.cis.hut.fi/projects/ica/fastica>). We concentrate on the results from the fast ICA, as the final results from both algorithms were similar and direct comparison of the performance of both algorithms is not the main concern of this paper (see Esposito et al., 2002). We briefly review the ICA algorithm below. For details of the theoretical descriptions and the computational implementations please refer to previous reports (Hyvarinen, 1999; Hyvarinen and Oja, 2000, for the fast ICA; Bell and Sejnowski, 1995; McKeown et al., 1998a,b, for the information-maximization algorithm).

Preprocessing

In each single session, the time-series data of all intracranial voxels are included in a data matrix, \mathbf{X} ; this is an n by m rectangular matrix, with n being the number of time points in a session and m being the total number of voxels sampled. Before running the ICA algorithm, data are centered and whitened (sphering). Each row of \mathbf{X}

is centered by subtracting the sample mean to make it a mean of zero. Next, the whitening transformation using the Eigenvalue decomposition of the covariance matrix of \mathbf{X} is applied to make each row of \mathbf{X} uncorrelated. This orthogonalization reduces the complexity of the problem to be solved by the ICA algorithm and prevents over-learning during training, as mentioned in the ICA literature. We performed a full Eigenvalue projection without dimension reduction to minimize the alteration of data. For simplicity of notation, we assume in the rest of this section that \mathbf{X} has been centered and whitened.

Decomposition

ICA assumes that spatially-independent components, \mathbf{C} , are derived from the data matrix, \mathbf{X} , by linear decomposition with an unmixing matrix, \mathbf{W} :

$$\mathbf{C} = \mathbf{W}\mathbf{X} \quad (1)$$

Here, \mathbf{C} is an n by m rectangular matrix, with n being the number of ICs and m being the total number of voxels, and \mathbf{W} is an n by n square matrix of full rank. We also define the mixing matrix, \mathbf{M} , as the inverse of \mathbf{W} , that is:

$$\mathbf{M} = \mathbf{W}^{-1} \quad (2)$$

The rows of \mathbf{M} represent the number of ICs and the columns give the time course of each component, the spatial distribution of which is provided by the row of \mathbf{C} . The problem to be solved by the ICA is to find \mathbf{W} that makes each column of $\mathbf{W}\mathbf{X}$ as mutually independent as possible. The fast ICA accomplishes this by maximizing the negentropy as the measures of the non-Gaussianity of the projected data $\mathbf{W}\mathbf{X}$ through the fixed-point iteration optimization (Hyvarinen, 1999). Once the fixed-point iteration is converged, we can obtain n spatially-independent component maps, as each row of $\mathbf{C} = \mathbf{W}\mathbf{X}$, and also calculate the mixing matrix $\mathbf{M} = \mathbf{W}^{-1}$, which represents the associated time course of each spatially-independent component map.

Appendix B

Multiple-regression analysis on the time series of the IC components (Fig. 2b)

The multiple-regression analysis was based on an ordinary GLM, the design matrix of which was constructed in accordance with the prespecified experimental design and is primarily the same as that used for voxel-by-voxel statistical analysis. It generally contains several task-related reference functions, trend functions (high-pass filters) and one constant term as follows:

$$\vec{m}_i = H\vec{\theta} + G\vec{\zeta} + B\vec{\zeta} + \vec{\eta} \quad (3)$$

Here, \vec{m}_i is the time course of the i th IC, or a $(n \times 1)$ vector of the i th column in a mixing matrix, \mathbf{M} , $\vec{\eta}$ is a $(n \times 1)$ vector representing a disturbance of this regression, and $\vec{\theta}$, $\vec{\zeta}$ and $\vec{\zeta}$ are vectors of the coefficient parameters for each column of a design matrix for the effects of interest (reference functions for hemodynamics), H , the nuisance effects (discrete cosine basis functions for the high-pass filter), G , and the block effects (constant term), B , respectively. After an ordinary least squares (OLS) estimation, the F test was performed to evaluate the

variance accounted for by the effects of interest as follows (Holmes et al., 1997; Friston et al., 1995c):

$$F_i = \frac{\frac{e_0^t e_0 - e_0^t e}{p - p_0}}{\frac{e_0^t e_0}{n - p_0}} \quad (4)$$

Here,

$$\vec{e}_0 = \vec{m}_i - H\vec{\theta}, p_0 = n - \text{rank}(H), \quad (5)$$

and

$$\vec{e} = \vec{m}_i - (H\vec{\theta} + G\vec{\xi} + B\vec{\zeta}), \quad (6)$$

Three estimates, $\vec{\theta}$, $\vec{\xi}$, and $\vec{\zeta}$, are the OLS-estimators of θ , ξ and ζ , respectively. The estimated residuals and the degrees of freedom for the F value are \vec{e} , p for the full model, and \vec{e}_0 , p_0 for the reduced model, respectively.

Appendix C

The BP test is a diagnostic test for heteroscedastic disturbances in a linear-regression model (Breusch and Pagan, 1979). As this test is carried out in the framework of the GLM with least-squares estimation, the application to neuroimaging data is as follows.

Consider a multiple-regression model,

$$Y_t = \beta_1 + \beta_2 X_{2t} + \cdots + \beta_k X_{kt} + u_t \quad (7)$$

($t=1, \dots, n$)

where X_{it} is a design matrix for the time-series data Y_t , β_i is a coefficient parameter, and the disturbance u_t is normally and independently distributed with a mean of zero and time-varying variance σ_t^2 . Here we assume that the heteroscedasticity of variance σ_t^2 could be modeled by the appropriate function f as:

$$\sigma_t^2 = f(\alpha_1 + \alpha_2 Z_{2t} + \cdots + \alpha_m Z_{mt}). \quad (8)$$

Here, Z_{it} is a new explanatory variable for the time series of σ_t^2 with the first element being unity, and α_i is a coefficient parameter of this regression. Although the form of function f is selected by experience, an integer power or exponential function is typically used. The element of Z_{it} in Eq. (8) is usually obtained from the explanatory variable X_{it} in Eq. (7), for example, X_{it} , X_{it}^2 or $X_{it}X_{jt}$ ($i \neq j$).

The null hypothesis of homoscedasticity is written as:

$$H_0: \alpha_2 = \cdots = \alpha_m = 0 \quad (9)$$

If this is correct, $\alpha_2 Z_{2t} + \cdots + \alpha_m Z_{mt} = 0$, thence $\sigma_t^2 = f(\alpha_1)$ is constant. Therefore, if at least one element of α_i is not 0, the tested time series Y_t is heteroscedastic. The χ^2 statistic, assuming the form of heteroscedasticity is as in Eq. (8), is computed as follows. Using the matrix notation, Eq. (7) is written as,

$$\vec{Y} = X\vec{\beta} + \vec{u} \quad (10)$$

where the first row value of X is unity. Applying the least-squares estimation, we obtain the estimated residual time series,

$$\vec{u} = R_X \vec{Y}, \quad (11)$$

where $R_X = I - X(X^T X)^{-1} X^T$ is a residual forming matrix. The estimated variance $\hat{\sigma}^2$ is estimated by:

$$\hat{\sigma}^2 = \hat{\vec{u}}^T \hat{\vec{u}} / n. \quad (12)$$

Calculate

$$\vec{p} = \hat{\vec{u}}^2 / \hat{\sigma}^2 \quad (13)$$

and then perform the regression of \vec{p} on Z

$$\vec{p} = Z\vec{\alpha} + \vec{v} \quad (14)$$

where \vec{v} is the disturbance term. It is noted that the first row of Z is unity. As the residual error sum of square for the full model Z under (9) is

$$SS_1 = (R_Z \vec{p})^T (R_Z \vec{p}) \quad (15)$$

where $R_Z = I - Z(Z^T Z)^{-1} Z^T$ and the residual error sum of square for the reduced model Z' specified by H_0 is

$$SS_0 = (R_{Z'} \vec{p})^T (R_{Z'} \vec{p}). \quad (16)$$

The explained sum of squares (SSE) defined as the partial contribution of parameters $\alpha_2 = \cdots = \alpha_m$ is

$$SSE = SS_0 - SS_1. \quad (17)$$

From the theorem of Breusch and Pagan, one half of the SSE is asymptotically distributed as χ^2 with $m-1$ degrees of freedom when the null hypothesis is true. The complete proof of this theorem is given in Breusch and Pagan (1979).

References

- Andersson, J.L., Hutton, C., Ashburner, J., Turner, R., Friston, K., 2001. Modeling geometric deformations in EPI time series. *NeuroImage* 13, 903–919.
- Arfanakis, K., Cordes, D., Haughton, V.M., Moritz, C.H., Quigley, M.A., Meyerand, M.E., 2000. Combining independent component analysis and correlation analysis to probe interregional connectivity in fMRI task activation datasets. *Magn. Reson. Imaging* 18, 921–930.
- Ashburner, J., Friston, K.J., 1999. Image registration. In: Moonen, A.T.W., Bandettini, P.A. (Eds.), *Functional MRI*. Springer, Berlin, pp. 285–299.
- Bannister, P., Beckmann, C., Jenkinson, M., 2001. Exploratory motion analysis in fMRI using ICA. Seventh International Conference on Functional Mapping of the Human Brain (Abstract). Academic Press, San Diego.
- Bell, A.J., Sejnowski, T.J., 1995. An information-maximization approach to blind separation and blind deconvolution. *Neural Comput.* 7, 1129–1159.
- Birn, R.M., Bandettini, P.A., Cox, R.W., Jesmanowicz, A., Shaker, R., 1998. Magnetic field changes in the human brain due to swallowing or speaking. *Magn. Reson. Med.* 40, 55–60.
- Birn, R.M., Bandettini, P.A., Cox, R.W., Shaker, R., 1999. Event-related fMRI of tasks involving brief motion. *Hum. Brain Mapp.* 7, 106–114.
- Biswal, B.B., Ulmer, J.L., 1999. Blind source separation of multiple signal sources of fMRI data sets using independent component analysis. *J. Comput. Assist. Tomogr.* 23, 265–271.
- Breusch, T.S., Pagan, A.R., 1979. A simple test for heteroscedasticity and random coefficient variation. *Econometrica* 47, 1287–1294.
- Bullmore, E.T., Brammer, M.J., Rabe-Hesketh, S., Curtis, V.A., Morris, R.G., Williams, S.C., Sharma, T., McGuire, P.K., 1999. Methods for diagnosis and treatment of stimulus-correlated motion in generic brain activation studies using fMRI. *Hum. Brain Mapp.* 7, 38–48.
- Calhoun, V.D., Adali, T., McGinty, V.B., Pekar, J.J., Watson, T.D., Pearlson, G.D., 2001. fMRI activation in a visual-perception task:

- network of areas detected using the general linear model and independent components analysis. *NeuroImage* 14, 1080–1088.
- Calhoun, V.D., Pekar, J.J., McGinty, V.B., Adali, T., Watson, T.D., Pearlson, G.D., 2002. Different activation dynamics in multiple neural systems during simulated driving. *Hum. Brain Mapp.* 16, 158–167.
- Chen, W., Zhu, X.H., 1997. Suppression of physiological eye movement artifacts in functional MRI using slab presaturation. *Magn. Reson. Med.* 38, 546–550.
- Duann, J.R., Jung, T.P., Kuo, W.J., Yeh, T.C., Makeig, S., Hsieh, J.C., Sejnowski, T.J., 2002. Single-trial variability in event-related BOLD signals. *NeuroImage* 15, 823–835.
- Esposito, F., Formisano, E., Seifritz, E., Goebel, R., Morrone, R., Tedeschi, G., Di Salle, F., 2002. Spatial independent component analysis of functional MRI time-series: to what extent do results depend on the algorithm used? *Hum. Brain Mapp.* 16, 146–157.
- Field, A.S., Yen, Y.F., Burdette, J.H., Elster, A.D., 2000. False cerebral activation on BOLD functional MR images: study of low-amplitude motion weakly correlated to stimulus. *Am. J. Neuroradiol.* 21, 1388–1396.
- Friston, K.J., Jezzard, P., Turner, R., 1994. Analysis of functional MRI time-series. *Hum. Brain Mapp.* 1, 153–171.
- Friston, K.J., Ashburner, J., Frith, C.D., Poline, J.B., Heather, J.D., Frackowiak, R.S.J., 1995a. Spatial registration and normalization of images. *Hum. Brain Mapp.* 3, 165–189.
- Friston, K.J., Holmes, A.P., Poline, J.B., Grasby, P.J., Williams, S.C., Frackowiak, R.S., Turner, R., 1995b. Analysis of fMRI time-series revisited. *NeuroImage* 2, 45–53.
- Friston, K.J., Holmes, A.P., Worsley, K.J., Poline, J.P., Frith, C.D., Frackowiak, R.S.J., 1995c. Statistical parametric maps in functional imaging: a general linear approach. *Hum. Brain Mapp.* 2, 189–210.
- Friston, K.J., Williams, S., Howard, R., Frackowiak, R.S., Turner, R., 1996. Movement-related effects in fMRI time-series. *Magn. Reson. Med.* 35, 346–355.
- Friston, K.J., Josephs, O., Zarahn, E., Holmes, A.P., Rouquette, S., Poline, J., 2000. To smooth or not to smooth? Bias and efficiency in fMRI time-series analysis. *NeuroImage* 12, 196–208.
- Grootoink, S., Hutton, C., Ashburner, J., Howseman, A.M., Josephs, O., Rees, G., Friston, K.J., Turner, R., 2000. Characterization and correction of interpolation effects in the realignment of fMRI time series. *NeuroImage* 11, 49–57.
- Holmes, A., Poline, J.B., Friston, K.J., 1997. Characterizing brain images with the General Linear Model. In: Frackowiak, R.S.J., Friston, K.J., Frith, C.D., Dolan, R.J., Mazziotta, J.C. (Eds.), *Human Brain Function*. Academic Press, San Diego, pp. 59–84.
- Hyvarinen, A., 1999. Fast and robust fixed-point algorithms for independent component analysis. *Trans. Neural Netw.* 10, 626–634.
- Hyvarinen, A., Oja, E., 2000. Independent component analysis: algorithms and applications. *Neural Netw.* 13, 411–430.
- Lee, C.C., Grimm, R.C., Manduca, A., Felmlee, J.P., Ehman, R.L., Riederer, S.J., Jack Jr., C.R., 1998. A prospective approach to correct for inter-image head rotation in fMRI. *Magn. Reson. Med.* 39, 234–243.
- McKeown, M.J., 2000. Detection of consistently task-related activations in fMRI data with hybrid independent component analysis. *NeuroImage* 11, 24–35.
- McKeown, M.J., Jung, T.P., Makeig, S., Brown, G., Kindermann, S.S., Lee, T.W., Sejnowski, T.J., 1998a. Spatially independent activity patterns in functional MRI data during the stroop color-naming task. *Proc. Natl. Acad. Sci. U. S. A.* 95, 803–810.
- McKeown, M.J., Makeig, S., Brown, G.G., Jung, T.P., Kindermann, S.S., Bell, A.J., Sejnowski, T.J., 1998b. Analysis of fMRI data by blind separation into independent spatial components. *Hum. Brain Mapp.* 6, 160–188.
- Moritz, C.H., Haughton, V.M., Cordes, D., Quigley, M., Meyerand, M.E., 2000. Whole-brain functional MR imaging activation from a finger-tapping task examined with independent component analysis. *Am. J. Neuroradiol.* 21, 1629–1635.
- Moritz, C.H., Rogers, B.P., Meyerand, M.E., 2003. Power spectrum ranked independent component analysis of a periodic fMRI complex motor paradigm. *Hum. Brain Mapp.* 18, 111–122.
- Seto, E., Sela, G., McIlroy, W.E., Black, S.E., Staines, W.R., Bronskill, M.J., McIntosh, A.R., Graham, S.J., 2001. Quantifying head motion associated with motor tasks used in fMRI. *NeuroImage* 14, 284–297.
- Worsley, K.J., Friston, K.J., 1995. Analysis of fMRI time-series revisited—Again. *NeuroImage* 2, 173–181.
- Yetkin, F.Z., Haughton, V.M., Cox, R.W., Hyde, J., Birn, R.M., Wong, E.C., Prost, R., 1996. Effect of motion outside the field of view on functional MR. *Am. J. Neuroradiol.* 17, 1005–1009.